

Simple interpretation of the seemingly complicated X-ray spectral variation of NGC 5548

Takuya Midooka^{1,2}, [★] Ken Ebisawa^{1,2}, Misaki Mizumoto^{3,4}, Yasuharu Sugawara¹

¹*Institute of Space and Astronautical Science (ISAS), Japan Aerospace Exploration Agency (JAXA), 3-1-1 Yoshinodai, Chuo-ku, Sagamihara, Kanagawa 252-5210, Japan*

²*Department of Astronomy, Graduate School of Science, The University of Tokyo, 7-3-1 Hongo, Bunkyo-ku, Tokyo 113-0033, Japan*

³*Hakubi Center, Kyoto University, Yoshida-honmachi, Sakyo-ku, Kyoto, 606-8501, Japan*

⁴*Department of Astronomy, Graduate School of Science, Kyoto University, Kitashirakawa-Oiwakecho, Sakyo-ku, Kyoto, 606-8502, Japan*

Accepted XXX. Received YYY; in original form ZZZ

ABSTRACT

NGC 5548 is a very well-studied Seyfert 1 galaxy in broad wavelengths. Previous multi-wavelength observation campaigns have indicated that its multiple absorbers are highly variable and complex. A previous study applied a two-zone partial covering model with different covering fractions to explain the complex X-ray spectral variation and reported a correlation between one of the covering fractions and the photon index of the power-law continuum. However, it is not straightforward to physically understand such a correlation. In this paper, we propose a model to avoid this unphysical situation; the central X-ray emission region is partially covered by *clumpy absorbers composed of double layers*. These “double partial coverings” have precisely the same covering fraction. Based on our model, we have conducted an extensive spectral study using the data taken by *XMM-Newton*, *Suzaku*, and *NuSTAR* in the range of 0.3–78 keV for 16 years. Consequently, we have found that the X-ray spectral variations are mainly explained by independent changes of the following three components; (1) the soft excess spectral component below ~ 1 keV, (2) the cut-off power-law normalization, and (3) the partial covering fraction of the clumpy absorbers. In particular, spectral variations above ~ 1 keV are mostly explained only by the changes of the partial covering fraction and the power-law normalization. In contrast, the photon index and all the other spectral parameters are not significantly variable.

Key words: accretion, accretion disks — galaxy: nucleus — galaxy: Seyfert — X-rays: individual: NGC 5548

1 INTRODUCTION

NGC 5548 is a typical well-studied Seyfert 1 galaxy, known to exhibit complicated X-ray spectral variations. It has complex and variable absorption features, and thus deep and multi-wavelength observation campaigns have been performed to reveal the surrounding structure around the central black hole. The “Anatomy of the AGN in NGC 5548” campaign covered the wide wavelength range from near-infrared to hard X-rays during 2013–2014 (e.g., [Kaastra et al. 2014](#)) and revealed the change of the absorbers’ structure and geometry. The “Space Telescope and Optical Reverberation Mapping Project” is a six-month-long reverberation-mapping experiment in 2014, which provided us with a deep insight into the broad line region (BLR) structure (e.g., [De Rosa et al. 2015](#)). In the “Anatomy” campaign, an outflowing stream of weakly ionized gas (called the “obscurer”), which had not been present until at least 2007, was recognized, causing the soft X-ray absorption and the broad UV absorption ([Kaastra et al. 2014](#)). [Kaastra et al. \(2014\)](#)

and [Arav et al. \(2015\)](#) also reported by spectral fitting of the Hubble Space Telescope UV data and *XMM-Newton* X-ray data that the warm absorber (WA) is composed of six-velocity components. Using the electron number densities and the ionization parameters, [Arav et al. \(2015\)](#) estimated locations of these components as a few pc to a few hundred pc from the central black hole.

NGC 5548 is one of the ideal sources to study gas structures around the AGN, thanks to its spectral variations and existence of the obscurer and the WA. For the “obscured” *XMM-Newton* and *NuSTAR* energy spectra during the Anatomy campaign, [Cappi et al. \(2016\)](#) applied a two-zone partial covering model with *different* covering fractions as well as other Anatomy campaign papers (e.g. [Ursini et al. 2015](#), [Di Gesu et al. 2015](#), and [Mehdipour et al. 2016](#)). [Cappi et al. \(2016\)](#) explained the spectral variation in 0.3–50 keV with the following nine free parameters; (1)–(6) column densities, partial covering fractions, and ionization parameters of the two partial absorbers, (7)–(8) power-law photon index and the normalization, and (9) the soft excess normalization. Interestingly, they reported a correlation between one of the covering fractions and the photon index of the power-law continuum, such that the power-law

[★] E-mail: midooka@ac.jaxa.jp

Table 1. Observation logs with *XMM-Newton* (pn), *Suzaku* and *NuSTAR*

Obs. Name	Satellite	Obs. ID	Start–End date [UT]	Exposure time (ks) ^a
*X1 ^b	<i>XMM-Newton</i>	0109960101	2000 Dec. 24–25	22.9
*X2	<i>XMM-Newton</i>	0089960301	2001 Jul. 09–10	83.0
*X3	<i>XMM-Newton</i>	0089960401	2001 Jul. 12–12	28.1
S1	<i>Suzaku</i>	702042010	2007 Jun. 18–19	31.1
S2	<i>Suzaku</i>	702042020	2007 Jun. 24–25	35.9
S3	<i>Suzaku</i>	702042040	2007 Jul. 08–08	30.7
S4	<i>Suzaku</i>	702042050	2007 Jul. 15–15	30.0
S5	<i>Suzaku</i>	702042060	2007 Jul. 22–22	28.9
S6	<i>Suzaku</i>	702042070	2007 Jul. 29–29	31.8
S7	<i>Suzaku</i>	702042080	2007 Aug. 05–05	38.8
*X4	<i>XMM-Newton</i>	0720110301	2013 Jun. 22–22	50.5
*X5	<i>XMM-Newton</i>	0720110401	2013 Jun. 30–30	55.1
*X6	<i>XMM-Newton</i>	0720110501	2013 Jul. 07–08	55.5
*X7	<i>XMM-Newton</i>	0720110601	2013 Jul. 11–12	55.4
*X7N ^c	* <i>NuSTAR</i>	60002044002/3	2013 Jul. 11–12	55.2
*X8	<i>XMM-Newton</i>	0720110701	2013 Jul. 15–16	55.5
*X9	<i>XMM-Newton</i>	0720110801	2013 Jul. 19–20	56.5
*X10	<i>XMM-Newton</i>	0720110901	2013 Jul. 21–22	55.5
*X11	<i>XMM-Newton</i>	0720111001	2013 Jul. 23–24	55.5
*X11N ^c	* <i>NuSTAR</i>	60002044005	2013 Jul. 23–24	53.1
*X12	<i>XMM-Newton</i>	0720111101	2013 Jul. 25–26	50.7
*X13	<i>XMM-Newton</i>	0720111201	2013 Jul. 27–28	55.5
*X14	<i>XMM-Newton</i>	0720111301	2013 Jul. 29–30	50.4
*X15	<i>XMM-Newton</i>	0720111401	2013 Jul. 31–Aug. 01	55.5
*X16	<i>XMM-Newton</i>	0720111501	2013 Dec. 20–21	55.3
*X16N ^c	* <i>NuSTAR</i>	60002044008	2013 Dec. 20–21	53.8
*X17	<i>XMM-Newton</i>	0720111601	2014 Feb. 04–05	55.4
X18	<i>XMM-Newton</i>	0771000101	2016 Jan. 14–14	35.2
X19	<i>XMM-Newton</i>	0771000201	2016 Jan. 16–16	32.5

^a Sum of all the good time intervals.

^b Those marked with “*” are used in [Cappi et al. \(2016\)](#).

^c Simultaneous observation by *XMM-NuSTAR*.

slope gets steeper while the covering fraction increases. Since the covering fraction is determined by the geometry of the distant partial absorbers from the central black hole, this correlation may not be explained physically. Although [Cappi et al. \(2016\)](#) mentioned the possibility of a parameter degeneracy, they proposed a physical interpretation: Assuming a disk-corona geometry similar to the one expected for Mrk 509 ([Petrucci et al. 2013](#)), increase in the accretion rate might decrease the inner radius of the corona due to disk recondensation (e.g. [Meyer-Hofmeister & Meyer 2006](#)), raising the effective covering fraction. Meanwhile, the accretion rate increase produces more UV photons, causing more effective cooling in the corona and softer spectra. Thus, a correlation between the covering fraction and the spectral index might be reproduced.

We suspect that the apparent correlation found by [Cappi et al. \(2016\)](#) is more likely due to parameter degeneracy between the photon index and the mildly-ionized partial absorber. In fact, when fitting a given CCD spectrum with increasing the partial covering fraction, the model soft X-ray photons are so decreased that the photon index has to get larger to compensate. To examine the possibility of parameter degeneracy, we need to constrain these parameters a priori in some manner. Here, we try the “variable double partial covering (VDPC) model” ([Miyakawa et al. 2012](#); [Mizumoto et al. 2014](#)) expecting to solve this problem. In this model, the line of sight is partially covered by clumpy absorbers composed of *double layers*; a thick/cold core and a thin/warm layer. Even if the intrinsic photon index is invariable, change of the partial covering fraction causes apparent spectral variations below ~ 10 keV. In this paper, we examine if the VDPC model can explain the seemingly com-

plicated 2013–2014 energy spectra of NGC 5548. Also, we apply the VDPC model to the X-ray spectra taken from 2000 to 2016 by *XMM-Newton*, *Suzaku*, and *NuSTAR* to study the long-term spectral variations of NGC 5548.

Below, in Section 2, we introduce the observation and data reduction. Next, we explain our spectral model and present the results of spectral fitting in Section 3. We also compare the observed Root Mean Square (RMS) spectra with the ones reproduced with the best-fit spectral model. In Section 4, we discuss application of the VDPC model to other objects, origin of the multi-component absorbers, and the long-term X-ray variation of NGC 5548.

2 OBSERVATIONS AND DATA REDUCTION

We used all the available archival data taken by *XMM-Newton* ([Jansen et al. 2001](#)), *NuSTAR* ([Harrison et al. 2013](#)), and *Suzaku* ([Mitsuda et al. 2007](#)) during 2000–2016, including three simultaneous observations by *XMM-Newton* and *NuSTAR* (Table 1).

In the analysis of the *XMM-Newton* data, we used the European Photon Imaging Camera (EPIC)-pn ([Strüder et al. 2001](#)) in 0.3–10.0 keV and the Reflection Grating Spectrometer (RGS; [den Herder et al. 2001](#)) in 0.4–2.0 keV. The EPIC-MOS data were not used because its effective area is lower than that of the pn detector. The pn and RGS data were reduced with SAS version 17.0.0 to obtain the filtered event files. Good time intervals were selected by removing the intervals dominated by flaring particle background when the count rate in 10–12 keV with PATTERN==0 is larger than

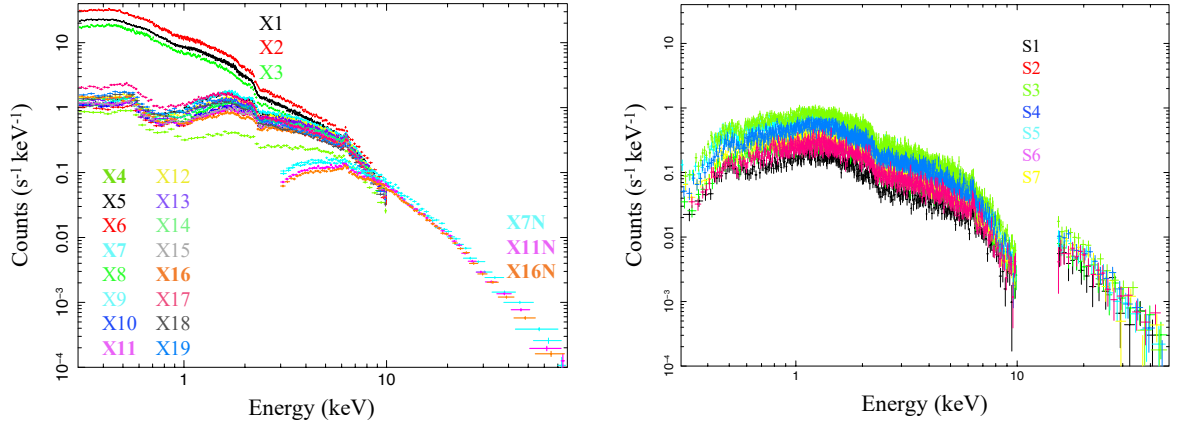


Figure 1. *Left:* All the archival spectra obtained by *XMM-Newton* pn in 0.3–10.0 keV and by *NuSTAR* in 3.0–78.0 keV. *Right:* All the archival spectra obtained by *Suzaku* XIS1 in 0.3–10.0 keV and by PIN in 15.0–50.0 keV. Detector responses are removed using the best-fit models.

0.4 counts s^{-1} for EPIC-pn data. We used circular regions of $30''$ radius and $45''$ radius from the same CCD for extracting the source events and the background events, respectively. Following the “SAS Data Analysis Threads”¹, we obtained the X-ray spectra and responses. The 1st-order spectra of RGS1 and RGS2 were combined.

To reduce the *NuSTAR* data, following the “*NuSTAR* Data Analysis Software Guide”², we used the standard pipeline `nupipeline` for reprocessing the data. The source events were extracted from circular regions within a $1.64'$ radius around the sources, and the background events were extracted from an annulus region of $2.87'–4.10'$ around the source. The spectra were extracted from the cleaned event files using the standard tool `nuproducts` for each of the two Focal Plane Modules (FPMA and FPMB). The FPMA and FPMB spectra were combined to provide better statistics using `addaspcaspec`.

In the *Suzaku* data analysis, we used the X-ray Imaging Spectrometer (XIS; Koyama et al. 2007) 0, 1, and 3 in 0.3–10.0 keV and Hard X-ray Detector (HXD; Takahashi et al. 2007). The HXD consists of two types of detectors, PIN and GSO, achieving a combined sensitivity in 10–600 keV. We used only the PIN detector in this study (15–50 keV) because our target is not bright enough in the GSO energy band. In the reduction of the XIS data, the source events were extracted from circular regions within a $2.0'$ radius of the sources, and the background regions were extracted from an annulus region of $3.0'–7.0'$ around the source. Spectra of the front-illuminated (FI) camera (XIS0 and XIS3) were combined by `addaspcaspec`. We adopted the “tuned background” as non X-ray background model of HXD-PIN³.

We grouped *XMM*-pn, *Suzaku*-XIS, and *NuSTAR* spectral bins so that each new bin holds more than 30 counts; similarly, 50 counts for *XMM*-RGS spectra and 500 counts for *Suzaku*-PIN spectra. Figure 1 shows the 0.3–78.0 keV spectra of all the currently available archival data with *XMM-Newton*, *NuSTAR*, and *Suzaku*. In this research, we used HEASOFT version 6.26 and XSPEC version 12.10.1f for spectral model fitting.

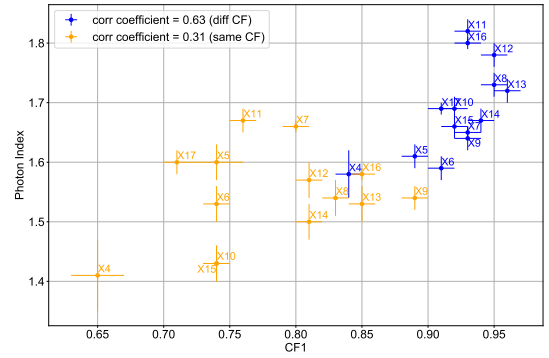


Figure 2. Photon index versus one of the two covering fractions CF1. Blue/orange markers show the fitting results obtained when the two covering fractions are independent/tied.

3 DATA ANALYSIS & RESULTS

Our primary goal is to explain the apparently complex spectral variations of NGC 5548 by a simple model with a minimum number of free parameters without parameter degeneracy. In Section 3.1, we reproduce the correlation between the power-law index and one of the covering fractions using the same two-zone partial covering model by Cappi et al. (2016), and study whether the degeneracy disappears letting the two covering fractions tied. In Section 3.2, we explain our VDPC model used in this study. We first apply the VDPC model to the three *XMM-NuSTAR* simultaneous spectra and the dimmest *XMM-Newton* spectrum to constrain the major parameters to characterize the spectral shape. We find these parameters are not significantly variable throughout the 16 year observation period. In Section 3.3, we apply these invariant parameters to all the archival data and extract variations of other spectral parameters.

3.1 Reproduction of the parameter correlation by Cappi et al. (2016)

First, we examine the *XMM-Newton* spectral dataset used by Cappi et al. (2016). Using the same two-zone partial covering model by

¹ <https://www.cosmos.esa.int/web/xmm-newton/sas-thread-epic-filterbackground>

<https://www.cosmos.esa.int/web/xmm-newton/sas-thread-pn-spectrum>
<https://www.cosmos.esa.int/web/xmm-newton/sas-thread-rgs>

² https://heasarc.gsfc.nasa.gov/docs/nustar/analysis/nustar_swguide.pdf

³ <https://heasarc.gsfc.nasa.gov/docs/suzaku/analysis/pinbgd.html>

Cappi et al. (2016), we fitted allowing the two covering fractions to vary independently. We used XSTAR version 2.2.1bn21 (Kallman et al. 2004) for the plasma simulation code, instead of the Cloudy code (Ferland et al. 2013) adopted by Cappi et al. (2016). As expected, we confirmed the reported correlation between one of the partial covering fractions (CF1) and the photon index, where the correlation coefficient is 0.63 (Figure 2, blue crosses). Next, we fitted the same dataset forcing the two covering fractions to be identical, then the correlation coefficient decreased to 0.31 (Figure 2, orange crosses). If we ignore an outlier (X4), the coefficient further drops to 0.08. Consequently, we suggest that the reported correlation is most likely due to the parameter degeneracy, and reduction of the free parameters can explain the spectral variation without any unphysical correlations.

3.2 Spectral fitting to the simultaneous *XMM-NuSTAR* spectra

We apply our VDPC model to the spectral data. First, we select the *XMM-NuSTAR* simultaneous spectra (X7, X7N, X11, X11N, X16, X16N in Table 1) and the dimmest *XMM-Newton* spectrum (X4) to constrain the main spectral parameters. Since both the power-law (cutoffPL) and the reflection components (pexmon) are dominant above ~ 10 keV, and effect of the partial absorption is most prominent in the dimmest spectrum, we expect to effectively constrain the overall spectral shape by fitting these spectra simultaneously.

The VDPC model adopted in this work is represented by the following equation:

$$F = [(P+B)(1-\alpha+\alpha W_1)(1-\alpha+\alpha W_2)W_3W_4 + R_{\text{Fe}} + I_{\text{gas}}]A \\ = [(P+B)\{(1-\alpha)(1-\alpha) + \alpha W_1(1-\alpha) + (1-\alpha)\alpha W_2 \\ + \alpha^2 W_1 W_2\}] * W_3 W_4 + R_{\text{Fe}} + I_{\text{gas}}]A,$$

where meaning of the parameters are explained below. The XSPEC representation is written as:

$$F = \{(\text{cutoffPL} + \text{diskbb})(1 - \text{const} + \text{const} * \text{mtable}_1) \\ * (1 - \text{const} + \text{const} * \text{mtable}_2) * \text{mtable}_3 * \text{mtable}_4 (2) \\ + \text{pexmon} + \text{mekal}\} * \text{phabs}.$$

A cut-off power-law component from the hot corona and the diskbb component from the optically thick accretion disk are the direct X-ray continua (see Figure 3). We suppose that the clumpy absorber has an internal double-layer structure that consists of a warm layer (W_1) and a cold core (W_2). These clumpy absorbers partially obscure the intrinsic continuum, where changes of the partial covering fractions in the line of sight are causing the apparent spectral variations. Then X-rays are fully absorbed by the ionized absorbers (W_3 and W_4) located farther from the center than the partial absorbers. Moreover, the power-law component is reflected by the outer accretion disk accompanying a narrow Fe emission line (pexmon). Besides these model components, there is a constant plasma thermal emission (mekal) that accounts for the emission lines in the soft X-ray band.

The cosmic redshift is 0.017 (Cappi et al. 2016), and we set the cosmic abundances to the wilms values (Wilms et al. 2000). Since the spectral slopes above ~ 10 keV looks very similar (Figure 1, left), we adopt a simple cut-off power-law model where the index and the cut-off energy are invariable. Cross-normalization constants between the three instruments (*XMM-pn*, *XMM-RGS*, and *NuSTAR-FPM*) were determined by the simultaneous fitting, resulting in the consistent values with Madsen et al. (2017).

We have tried to fit the seven spectra of the four observations

simultaneously with minimum free parameters. Consequently, we have found that these observations can be explained without varying the power-law index significantly, and the reflection component and the multiple absorber parameters at all (Table 2 and Figure 4). The power-law photon-index can be the same at 1.54, besides the dimmest observation (X4), 1.39. In Table 2, we show the best-fit parameters common to the four observations. Other variable parameters are shown in Table 3. Figure 4 shows the results of the fitting in 0.3–78.0 keV, where the reduced chi-square value is 1.24 (d.o.f. = 9418).

The following is explanation of the individual model components in equations (1) and (2):

(i) *Interstellar absorption*: A/phabs : $\exp(-N_{\text{H}}\sigma(E))$
 N_{H} and $\sigma(E)$ are the hydrogen column density along the line of sight and the photoelectric absorption cross section as a function of the X-ray energy, respectively. The column density was fixed at the Galactic value $N_{\text{H}} = 1.55 \times 10^{20} \text{ cm}^{-2}$ (Bekhti et al. 2016).

(ii) *Cut-off power-law*: $P/\text{cutoffPL}$: $KE^{-\Gamma} \exp(-E/E_{\text{cut}})$
 K is the normalization in [photons/keV/cm²] at 1 keV, Γ is the photon index and E_{cut} is the cut-off energy. We assume that the power-law component is emitted from the hot corona around the central black hole (Figure 3).

(iii) *Partial absorption by “cold clumps”*: $W_{1,2}/\text{mtable}_{1,2}$: $\exp\{-\sigma(E, \xi)N_{\text{H}}\}$

These are the essential components in the VDPC model and correspond to the “obscurer” recognized in the “Anatomy” campaign observation (Kaastra et al. 2014). The mtable models describe transmission by ionized absorbers as a function of the column density N_{H} and the ionization parameter ξ , calculated with XSTAR. We adopt the 20×20 parameter grids in the range of $0.1 < \log(\xi / \text{erg cm s}^{-1}) < 5$ and $20 < \log(N_{\text{H}} / \text{cm}^{-2}) < 25$ in logarithmic steps. We fix the gas temperature at 10^5 K, the gas density at $1.1 \times 10^{12} \text{ cm}^{-3}$, and the turbulent velocity at 200 km s^{-1} . Abundances are fixed to the solar values except for those minor elements (Be, Ba, Na, Al, P, Cl, K, Sc, Ti, V, Cr, Mn, Co, Cu, and Zn) that are ignored to simplify the calculation. The incident spectrum is assumed to be a power-law with the photon index 2.0. Effects of changing the intrinsic spectra are estimated in the final paragraph of this section.

Combination of the fixed mtable and the variable covering fraction α/const represents the partial absorption. We need two different ionized partial absorbers, which have the same α . These partial absorbers are presumably due to double-layered cold clumps (Figure 3). We will discuss physical interpretation of these absorbers in detail in Section 4.1.

(iv) *Full absorption by “ionized absorber”*: $W_{3,4}/\text{mtable}_{3,4}$: $\exp\{-\sigma(E, \xi)N_{\text{H}}\}$

These two components cause the ionized full-covering absorption (Figure 3), which approximate several components of WAs. Cappi et al. (2016) noted that the six-component WAs reported in Kaastra et al. (2014) are approximated by two components during the unobscured period and that influence of the multi-components is weaker during the obscured period. We applied average values of the two WAs by Cappi et al. (2016) to the invariable components W_3 and W_4 .

(v) *Cold reflection with Fe line*: $R_{\text{Fe}}/\text{pexmon}$
This is a Compton reflection component from cold outer-part of the accretion disk, including the narrow fluorescence lines (pexmon; Nandra et al. 2007). We fixed the disk inclination angle at $i = 30^\circ$, where it was suggested as $i = 38.8_{-11.4}^{+12.1}^\circ$ (Pancoast et al. 2014) or $36 \pm 10^\circ$ (Starkey et al. 2017). We determined the redshift value by

the simultaneous fitting considering the line shift from the cosmic value due to an ionized disk or a kinetic Doppler shift. Since the observed fluorescent Fe $K\alpha$ line strength does not vary significantly compared to the continuum variation, we have fixed the `pexmon` normalization in the simultaneous fitting.

(vi) *Soft excess: B/diskbb*

Several interpretations exist for the soft excess component, e.g., the optically thick Comptonized disk model (Done et al. 2012). In this paper, we assume a black body accretion disk model for simplicity (`diskbb`; Mitsuda et al. 1984; Makishima et al. 1986). The `diskbb` has two parameters, temperature at the inner edge of the accretion disk kT_{in} and normalization ($= r_{\text{in}}^2 \cos i / d_{10\text{kpc}}$), where r_{in} , $d_{10\text{kpc}}$, and i are the innermost radius of the disk, the distance in the unit of 10 kpc, and the disk inclination angle, respectively. In most cases of NGC 5548, only the soft excess tail is observed below ~ 1 keV, and the temperature and the normalization are hardly constrained simultaneously. Thus, we fixed the `diskbb` normalization, and varied only kT_{in} .

(vii) *Thermal plasma emission: I_{gas}/mekal*

The soft excess component has not only the continuum emission but also the emission lines. We modeled the emission-line component using the thermal plasma radiation model `mekal`. Since one-temperature `mekal` does not accurately describe the observed spectrum, we apply two-temperature `mekal` in this study. This component has been constant throughout the 16-year observation. The hot plasma is considered to originate either in the host galaxy or in the narrow line region (e.g., Whewell et al. 2015; Cappi et al. 2016).

In the actual multi-absorber scenario, we note that the first absorber would alter the input spectrum to the second one, and so does the second one to the input spectrum to the third one, and so on. Thus, it would be ideal to carry out such successive photoionization calculation that a preceding absorber’s output spectrum is incident to the following absorber. However, this is not so easy that we have adopted such a simple approximation that the incident spectrum to the absorbers is a static power-law function.

Below, we evaluate the validity of this approximation. We investigate whether the spectral fitting results are dependent on XSTAR table models (`mtab1e`) created with different incident spectra. Table 2 shows the best-fit parameters using the table model created with the photon index 2.0. We created new table models with the input photon indices 1.5 and 2.5, and repeated the same simultaneous fitting replacing the tables. Consequently, we found that the fitting results are almost identical (the reduced chi-square values are 1.26 and 1.22, respectively, as opposed to the original one, 1.24), and the residual patterns are not distinguishable. Best-fit parameter values are invariable within statistical uncertainty, besides those of the partial absorber parameters (N_{H} and $\log \xi$ for W_1 and N_{H} for W_2). The new best-fit values are the following (in the order of the photon-indices 1.5 and 2.5): For W_1 , ($N_{\text{H}} / 10^{22}\text{cm}^{-2}$)=1.17 and 1.05, $\log(\xi / \text{erg cm s}^{-1})$ =0.93 and 0.1. For W_2 , ($N_{\text{H}} / 10^{22}\text{cm}^{-2}$)=2.46 and 3.04. These differences are minor, and we conclude that our approximation of the constant incident spectra to the multi-absorbers is valid to represent the picture depicted in Figure 3.

3.3 Fitting of all the available spectra

We have shown in the previous section that the four spectra in the 2013 campaign (X4, X7, X11, and X16) including the brightest (X7) and the dimmest (X4) ones are explained without varying the main spectral shape and the multiple absorber parameters (Table 2 and Figure 4). Most variable parameters are (1) the partial covering

Table 2. Spectral parameters determined by simultaneous fitting in 0.3–78.0 keV of the seven spectra from three simultaneous observations by *XMM-Newton* (X7, X11, X16) and the dimmest observation by *XMM-Newton* (X4). Model details are explained in Section 3.2. The parameters shown in this table are common in the four observations, X4, 7, 11, and 16, except for `cutoffPL` Γ . The photon index of X4 is smaller than those of the other observations and cannot be fitted well with the tied value. The error ranges correspond to the 90% confidence level throughout this paper.

	Model	Parameters	Best-fit values
A	<code>phabs</code>	N_{H} (10^{20}cm^{-2})	1.55 (fixed)
W_1	warm-layer absorber	N_{H} (10^{22}cm^{-2})	1.10 ± 0.05
		$\log \xi$	0.40 ± 0.02
W_2	cold-core absorber	N_{H} (10^{22}cm^{-2})	2.70 ± 0.04
		$\log \xi$	0.10 (fixed)
W_3	ionized absorber	N_{H} (10^{22}cm^{-2})	0.24 (fixed)
		$\log \xi$	1.07 (fixed)
W_4	ionized absorber	N_{H} (10^{22}cm^{-2})	0.66 (fixed)
		$\log \xi$	2.70 (fixed)
P	<code>cutoffPL</code>	Γ (X7,X11,X16)	$1.54_{-0.02}^{+0.01}$
		Γ (X4)	1.39 ± 0.02
		E_{cut} (keV)	$72.8_{-5.0}^{+5.3}$
R_{Fe}	<code>pexmon</code>	Γ	= <code>cutoffPL</code> Γ
		abund	1.0 (fixed)
		redshift	0.009 ± 0.001
		norm (10^{-3})	2.5 ± 0.2
B	<code>diskbb</code>	norm (10^3)	$44.0_{-6.5}^{+7.5}$
I_{gas}^a	<code>mekal₁</code>	kT (keV)	0.142 ± 0.008
		norm (10^{-4})	3.3 ± 0.6
	<code>mekal₂</code>	kT (keV)	0.623 ± 0.026
		norm (10^{-4})	0.82 ± 0.08

^a The `mekal` parameters were determined only from X4 since they are hardly constrained in other spectra due to confusion of other spectral components.

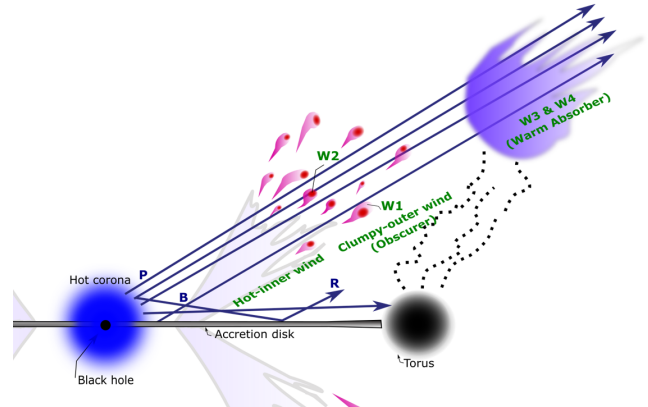


Figure 3. Schematic view of our picture around the black hole and accretion disk (not in scale). The intrinsic X-rays of `cutoffPL` (P in the figure) and `diskbb` (B) are emitted from the hot corona around the central black hole and the inner accretion disk, respectively. These intrinsic X-rays are partially covered by the “cold clumps”, each of which consists of two layers; a cold core (W_2) and warm layer (W_1). These cold clumps, known as “obscurers”, cause the “double partial covering” with the same covering fraction. The cold clumpy-outer wind is likely to be a consequence of the putative hot-inner wind that is hardly recognized probably because too hot and/or optically thin. All the X-rays are fully absorbed by the outer WAs (W_3 and W_4), which are formed from the ionized material due to evaporation of the irradiated torus.

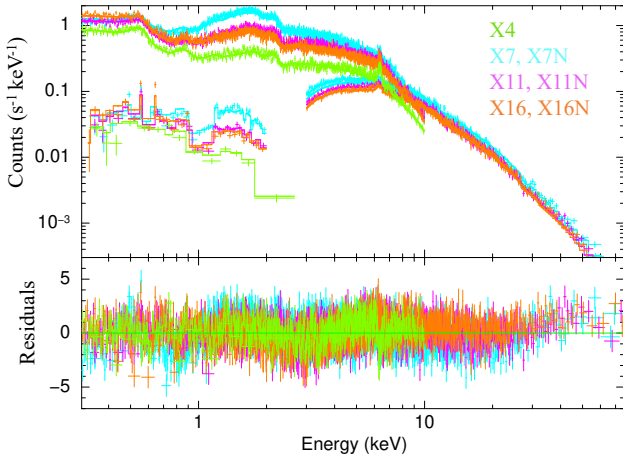


Figure 4. Spectral fitting of the three simultaneous observations by *XMM-NuSTAR* (X7, X11, X16) and the dimmest observation by *XMM-Newton* (X4) within 0.3–78.0 keV. The upper panel shows the observed spectra and the best-fit model (see table 2). The lower panel shows residuals of the model fitting.

fraction, (2) the power-law normalization and (3) the *diskbb* temperature (Table 3). We examine if similar spectral fitting is possible for all the other observations with minimum numbers of the variable parameters.

We fit each of all the observations individually with minimum variable parameters in addition to the three free-parameters in the 2013 *XMM-NuSTAR* campaign. First, we found no significant variations in the iron emission line and the reflection component (*pevmon*). We also found that the spectra taken during the unobscured period (X1, X2, and X3 in 2000–2001) had clearly different characteristics from those taken in 2007 and afterward. These unobscured spectra were much brighter than others below ~ 2 keV (Figure 1), where the covering fraction was null. They required a higher photon index and a lower soft excess normalization than the 2013 *XMM-NuSTAR* campaign. These results suggest that the physical conditions of the hot corona and the inner accretion disk had significantly varied in the time-scale of years between 2001 and 2007, whereas the outer disk reflection is invariable in this time-scale.

For all the other spectra in 2007 and afterward, the same index (1.54) as in the simultaneous fitting is valid beside the faintest spectrum X4 which requires a lower photon-index (1.39). The *diskbb* normalization was also fixed to the value determined from the *XMM-NuSTAR* simultaneous fitting. We show all the results of the model fitting in Figure A.1 (for *Suzaku*) and Figure A.2 (for *XMM-Newton*). The best-fit parameters are shown in Table 3. Some spectra (e.g., X5, X15 and X17) exhibit local residual feature below ~ 1 keV, which would suggest a minor variation of the absorbers. Besides, major variable parameters over the entire ~ 16 year period are (1) the covering fraction α , (2) the *cutoffPL* normalization, and (3) the *diskbb* temperature kT_{in} , as in the 2013 *XMM-NuSTAR* campaign. We emphasize that all the model fits are reasonable with such a simple model with little changes in the intrinsic spectra and absorbers' parameters.

We point out that the observation X4, which was the faintest in the *XMM-Newton* observations, returns a photon index of 1.39, that seems extremely hard. Such low photon-indices in extreme low states have been also reported in other Seyfert galaxies (e.g.,

Pounds et al. 2004). It is possible that the the AGN corona may have a tendency to get hotter and/or thicker when getting dimmer.

During the *Suzaku* observation period (June to August 2007), the covering fraction was tiny (< 0.05) or null, which may imply that the obscurer started to emerge at around that time. While previous studies (e.g., Liu et al. 2010; Krongold et al. 2010) analyzing the same *Suzaku* data have not reported the presence of the obscurer, Kaastra et al. (2014) argued that the obscuration may have started between August 2007 and February 2012, when *Swift* was not monitoring NGC 5548.

3.4 Reproduction of RMS spectra with the best-fit model

In this section, we try to explain the observed RMS spectra with the best-fit spectral model obtained in the previous section. The RMS spectra show fractional variations as a function of the X-ray energy, that intuitively informs us which components primarily contribute to the spectral variability.

Following Edelson et al. (2002), the RMS spectra were calculated from the observed and best-fit model spectra for each *XMM-Newton* observation with the 0.1 keV energy bins between 0.3–10.0 keV. Figure 5 shows the observed and model RMS spectra. The left one shows the RMS spectra from all the observations including the unobscured period (X1–X3), and the right is calculated from only X4–X19 in the obscured period.

In both figures, the dip around 6.4 keV indicates that the neutral Fe line from the outer-disk reflection is relatively constant compared to other spectral components. In the left figure, the variations are as large as $\sim 200\%$ below 1 keV, which is due to the emergence of the obscurers after 2007. In the right figure, where most variations are due to change of the partial covering fraction, the RMS spectrum is characterized by a broad peak around ~ 1 keV. This is because the partial absorber is most opaque just below the Fe-L edge, thus variation of the partial covering fraction most affects the spectral variation at around ~ 1 keV (see also Figure 7). Similar ~ 1 keV peaks are recognized from RMS spectra of other Seyfert 1 galaxies, where partial covering is dominant (e.g., Yamasaki et al. 2016).

4 DISCUSSION

We have found that the VDPC model, where two partial absorbers have exactly the same covering fraction, can explain the long-term spectral variations and RMS spectra of NGC 5548. This model is shown to be also valid for other Seyfert galaxies in precedent works (Miyakawa et al. 2012; Mizumoto et al. 2014; Iso et al. 2016; Yamasaki et al. 2016). Below, we discuss physical origin and implication of the VDPC model.

4.1 Mathematical and Physical description of the VDPC model

The mathematical VDPC representation is described in Equation 1, which indicates a situation that the central X-ray emitting region is sequentially obscured by the partial absorbers W_1 and W_2 having the same covering fraction and fully covered by the full-absorbers W_3 and W_4 . The upper diagram in Figure 6 literally illustrates this situation. The key point of the VDPC model is that the two partial absorbers W_1 and W_2 have exactly the same and *variable* covering fractions. However, it is very challenging to assume that the two independent absorbing layers accidentally have the same covering fraction and always vary in sync.

Table 3. Variable parameters determined by the spectral fitting with *XMM-Newton* (pn, RGS) and *Suzaku* (XIS0, 1, 3, PIN). Other parameters common to all the spectra are shown in Table 2. Those parameters without error values are the fixed ones.

Obs.	fitting results (refer Section 3.3)					computed flux (refer Section 4.2)		
	α	diskbb kT_{in} (eV)	diskbb norm (10^3)	PL norm (10^{-3})	PL index	χ^2/dof	diskbb flux ^a ($10^{-12}\text{erg/s/cm}^2$)	PL flux ^b ($10^{-12}\text{erg/s/cm}^2$)
X1	0	162±3	1.21±0.09	8.4±0.1	1.70	1.17	1.4±0.1	129±1.5
X2	0	176±1	0.83±0.03	10.5±0.1	1.70	1.41	0.9±0.1	161±1.5
X3	0	186±2	1.04±0.05	13.8±0.1	1.70	1.33	1.8±0.1	211±1.5
S1	0.02 ^{+0.02} _{-0.01}	57 ⁺² ₋₃	44.0	1.6±0.1	1.54	1.03	27.8±5.9	24±1.5
S2	0.02±0.01	50	44.0	2.8±0.1	1.54	1.06	16.4	43±1.5
S3	0	72±1	44.0	6.0±0.1	1.54	1.31	70.7±3.9	92±1.5
S4	0.04±0.01	62±2	44.0	3.7±0.1	1.54	1.06	38.9±7.5	57±1.5
S5	0	71±1	44.0	7.4±0.1	1.54	1.10	66.8±3.8	113±1.5
S6	0	55 ⁺⁴ ₋₉	44.0	4.7±0.1	1.54	1.06	24.1±8.8	72±1.5
S7	0.05±0.01	55 ⁺³ ₋₅	44.0	2.5±0.1	1.54	1.08	24.1±3.5	38±1.5
X4	0.96±0.01	137±1	44.0	2.4±0.1	1.39±0.01	1.13	926.6±27.1	37±1.5
X5	0.71±0.01	50	44.0	7.5±0.1	1.54	1.36	16.4	115±1.5
X6	0.76±0.01	74±1	44.0	5.2±0.1	1.54	1.21	78.9±4.3	80±1.5
X7	0.73±0.01	50	44.0	8.2±0.1	1.54	1.38	16.4	125±1.5
X8	0.78±0.01	78±1	44.0	6.7±0.1	1.54	1.21	97.4±5.0	103±1.5
X9	0.81±0.01	84±1	44.0	6.4±0.1	1.54	1.29	131.0±6.2	98±1.5
X10	0.77±0.01	77±1	44.0	5.5±0.1	1.54	1.42	92.5±4.8	80±1.5
X11	0.95±0.01	146±1	44.0	6.2±0.1	1.54	1.19	1195.1±32.7	95±1.5
X12	0.74±0.01	78±1	44.0	7.3±0.1	1.54	1.32	97.4±5.0	112±1.5
X13	0.75±0.01	78±1	44.0	7.2±0.1	1.54	1.25	97.4±5.0	110±1.5
X14	0.74±0.01	78±1	44.0	6.4±0.1	1.54	1.31	97.4±5.0	98±1.5
X15	0.77±0.01	80±1	44.0	5.6±0.1	1.54	1.48	107.7±5.4	86±1.5
X16	0.94±0.01	142±1	44.0	5.4±0.1	1.54	1.28	1069.4±30.1	83±1.5
X17	0.59±0.01	69±1	44.0	6.1±0.1	1.54	1.70	59.6±3.5	93±1.5
X18	0.63±0.01	64±1	44.0	5.0±0.1	1.54	1.34	44.1±2.8	77±1.5
X19	0.62±0.01	66±1	44.0	5.4±0.1	1.54	1.27	49.9±3.0	83±1.5

^a Bolometric fluxes of diskbb without any absorption.

^b cutoffPL fluxes without any absorption in 0.3–50.0 keV assuming the best-fit parameters $\Gamma = 1.54$ and $E_{\text{cut}} = 72.8$ keV.

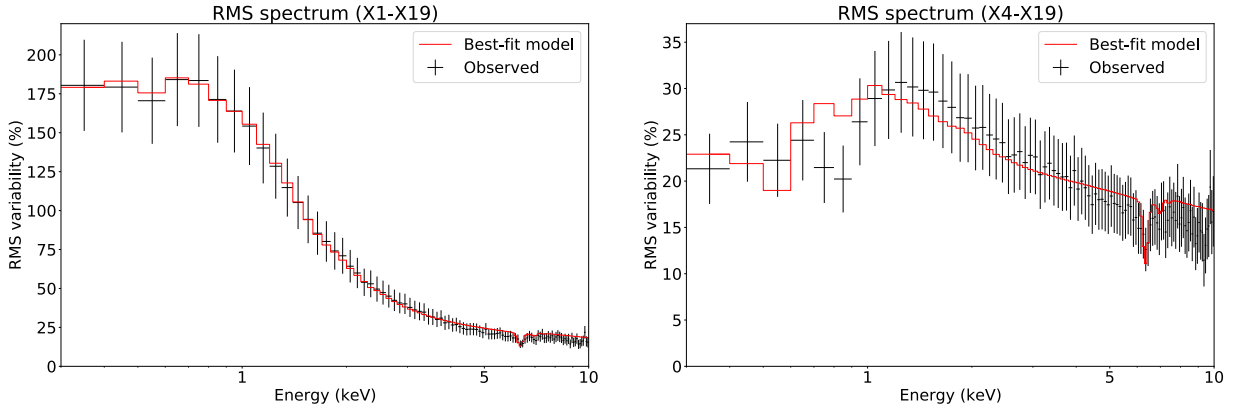


Figure 5. RMS spectra calculated from the observed spectra (black) and the best-fit model spectra (red). Observations used for RMS calculation are X1–X19 (left) and only X4–X19 (right), respectively.

Therefore, we suppose that “double-layer clumpy absorbers” are more plausible, as in the lower illustration of Figure 6. In this case, it is naturally understood that the two absorbers have the same covering fraction. The only difference is in those X-rays indicated with the blue lines in the figure; in the top panel, they are intervened only by the core of the clump (W_2), but they are necessarily intervened by the outer-layer of the clump (W_1) in the bottom panel. However, since W_1 is much optically thinner than W_2 , the additional W_1 absorption is not very significant (see Figure 7). Thus,

the double-layer absorbers in the bottom panel practically satisfy Equation 1.

4.2 Comparison with other objects

Previous studies suggest presence of the multi-layer/clumpy absorbers in other Seyfert galaxies besides NGC 5548. For example, NGC 3783 exhibits heavy eclipsing events, which can be naturally explained by two partially covering components with similar covering fractions (Mehdipour et al. 2017). In the case of NGC 1365,

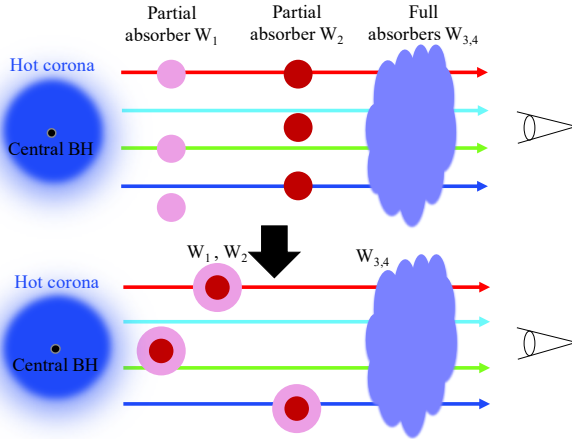


Figure 6. Schematic drawings of the absorbers with the VDPC model. *Upper:* Faithful schematic description of the absorbers. The same fraction of the X-rays (in this case 50 %) are absorbed by the two independent absorbing layers, W_1 and W_2 . *Lower:* More realistic configuration of the absorbers.

Maiolino et al. (2010) proposed that partial absorbers are likely to be cometary-shape clouds, consisting of a high-density head and an elongate tail with lower density. NGC 4051 is a bright AGN, in which variability of the individual emission/absorption lines have been studied in detail (Mizumoto & Ebisawa 2017). Its spectrum was explained by an invariable ionized absorber and variable double-layer clumpy absorbers, where the ionized absorber comprises two plasma components with different velocities and ionization states (Mizumoto & Ebisawa 2017). Thus, a picture of the “invariable ionized absorber” and the “variable double-layer clumps” seems to be common, while these absorbers’ parameters are different depending on individual AGN circumstances. Besides AGN, Hirsch et al. (2019) found that the clumpy stellar winds of Cyg X-1 cause partial covering, where each clump consists of a cool and dense matter embedded in outer photoionized layer.

4.3 Origin of the multiple absorbers

We have seen that X-ray spectral variation of NGC 5548 is naturally understood by introducing invariable ionized absorbers (W_3 and W_4) and variable double-layer clumpy absorbers (W_1 and W_2). The former corresponds to the “warm absorber” (WA; e.g., Kaastra et al. 2000) and the latter corresponds to the “obscurer” (e.g., Kaastra et al. 2014) in previous studies.

It is being recognized that “outflow” is a common phenomenon in accreting systems such as AGNs and X-ray binaries. In fact, global radiation-magnetohydrodynamic simulations (e.g., Takeuchi et al. 2013; Kobayashi et al. 2018) predict emergence of the clumpy outflow mostly due to the Rayleigh-Taylor instability. The disk wind outflow is hotter near the accretion disk, then cooled down as it moves farther away, transforming into the clumpy-outer wind at several hundred times the Schwarzschild radius. These clumpy-outer winds are likely origins of the double-layer obscurers.

The “hot-inner and clumpy-outer wind” picture successfully describes the characteristic broad Fe-K line shape and the time-lags commonly observed from narrow-line Seyfert galaxies such as 1H0707-495 (Mizumoto et al. 2019a). In the case of these high-mass accretion rate systems, the fast and thick hot-inner wind would

produce the blue-shifted Fe-K absorption lines (e.g., Hagino et al. 2015) and/or scatter X-rays to produce P-Cygni like broad features (e.g., Hagino et al. 2016; Mizumoto et al. 2019a). On the other hand, such strong Fe-K features are not seen in the X-ray spectra of NGC 5548, presumably because the inner-wind may be fully ionized and/or optically thin. Here, we instead suggest a possibility of the thermal wind origin of the WA (e.g., Krolik & Kriss 2001; Mizumoto et al. 2019b). Materials in the outer-torus or accretion flow are heated by X-rays, and evaporated to produce thermally driven outflows (Figure 3). These ionized outflows with moderate velocities in the line-of-sight are presumably the WAs’ origin to produce the X-ray and UV absorption lines.

The unified AGN model assumes the BLR clouds obscured by the dust torus (e.g., Antonucci & Miller 1985; Urry & Padovani 1995). However, physical origin, geometry, and dynamics of the BLR clouds are still under discussion. Thus, relationship between the clumpy outer winds (obscures) of the VDPC model and the BLR clouds has not been fully elucidated. On one hand, Miyakawa et al. (2012) estimated the size and location of the partial absorbers and suggested that the partial covering clouds in the VDPC model are consistent with the BLR clouds. Similarly, Matthews et al. (2020) reproduced the BLR-like spectra assuming clumpy biconical disk winds illuminated by an AGN continuum. Maiolino et al. (2010) also claimed that the cometary clouds’ parameters are consistent with those of the BLR clouds. On the other hand, Kaastra et al. (2014) argued that the obscurer in NGC 5548 should be farther away from the BLR because it partially absorbed the broad emission lines. According to the reverberation mapping observations of the STORM campaign (e.g., Williams et al. 2020), the radius of the NGC 5548 BLR is estimated to be several hundred times the Schwarzschild radius. Simulation by Kobayashi et al. (2018) predicted presence of the clumpy-outer winds farther than several hundred times the Schwarzschild radius, which corresponds to the position equal to or farther than the BLR. Therefore, we suppose the clumpy absorbers in NGC 5548 either correspond to the outer BLR clouds or are located beyond the BLR clouds.

4.4 Variation of the spectral parameters over 16 years

Figure 7 shows two representative energy spectra with similar continuum emissions but completely different partial covering fractions. The left shows the X11 data obtained by *XMM-NuSTAR*, and the right shows the S4 data obtained by *Suzaku* XIS1-PIN. They have the same `diskbb` normalization and low temperatures ($T_{\text{in}} \approx 50\text{--}150$ eV), which causes a minor spectral difference below ~ 1 keV. Changes of the power-law normalization have little influence on the spectral shape. Namely, spectral changes above ~ 1 keV are essentially caused by only changes of the covering fraction. The covering fractions of X11 and S4 are 0.95 and 0.04, respectively. As seen in Figure 7, the apparent change of the entire spectrum is mostly explained by only variation in the covering fraction.

In this study, the power-law photon index Γ is invariable between 2007 and 2016, except for X4. This might sound inconsistent with the widely-accepted “softer-when-brighter” trend of Seyfert galaxies (e.g., Sobolewska & Papadakis 2009; Soldi et al. 2014; Liu et al. 2021; Laurenti et al. 2022). We point out that considering the partial absorption, larger covering fractions cause a reduction of the soft X-rays and apparently flat spectra even when the intrinsic photon index is invariable. Thus, we suggest that the apparent softer-when-brighter trend is explained by a change of the partial covering fraction, at least to some extent.

The `diskbb` flux F_{disk} is obtained by the relation $F_{\text{disk}} =$

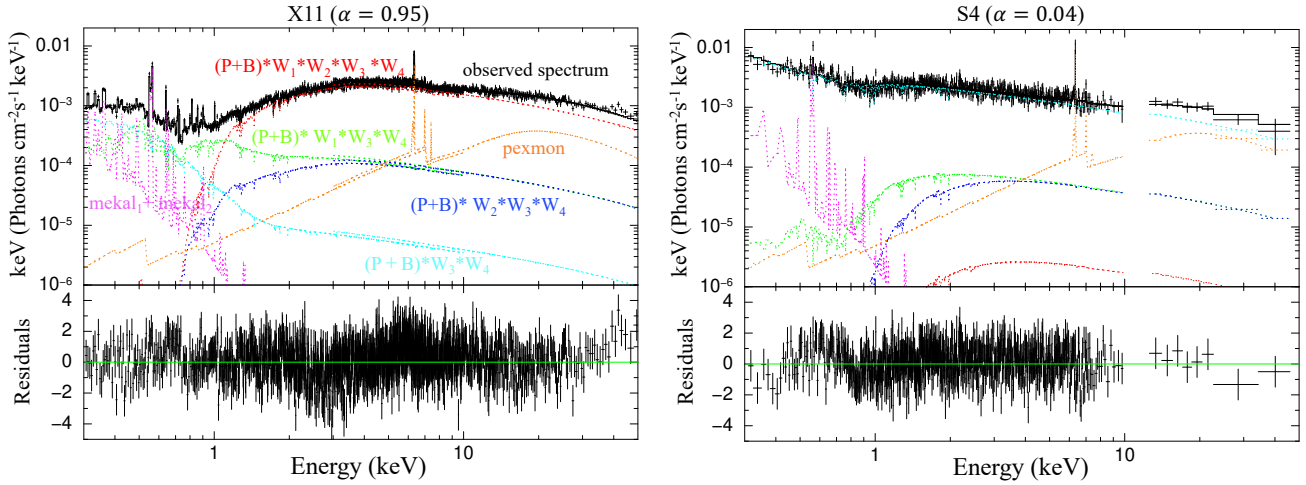


Figure 7. Spectral fitting results of a representative simultaneous observation by *XMM-NuSTAR* (X11; left) and by *Suzaku* XIS1-PIN (S4; right) within 0.3–50.0 keV. On the upper panel of both figures, black solid line is the best-fit model spectrum and the dotted-lines show individual continuum components. Those spectral components colored in light-blue, blue, green and red correspond to those with the same colors in the top-panel of Figure 6. Among all the four component going through the full absorbers (W_3 and W_4), the light-blue component is neither absorbed by the warm layer (W_1) nor the cold core (W_2). Blue and green components are absorbed only by the cold core and the warm layer, respectively. Red one is absorbed by both absorbers. Note that the red component and the blue component are hardly distinguishable in shape, since W_1 is much optically thinner than W_2 . Orange and magenta dotted-lines describe the outer-disk reflection (pexmon) and the thermal plasma component (two-temperature mekal), respectively. The vertical axes show energy flux. The spectra are unfolded around the best-fit model using the XSPEC command `eufspec`.

$L_{\text{disk}} \cos i / 2\pi d^2$, where $L_{\text{disk}} = 4\pi r_{\text{in}}^2 \sigma T_{\text{in}}^4$, d is the distance to NGC 5548, 71.77 Mpc. We also calculated `cutoffPL` flux of the 0.3–50.0 keV band using the XSPEC `flux` command. These `diskbb` and `cutoffPL` fluxes are shown in Table 3, which may be combined to estimate the total unobscured continuum flux from the central region. The `diskbb` flux is significantly variable, but its spectrum is too soft to highly ionize those heavy elements that are ionized mainly by the hard power-law photons. As shown in Table 3, the `cutoffPL` flux does not vary much, which justifies our early assumption that ionization parameters of the intervening matters are invariable.

Figure 8 shows variations of the partial covering fraction and the total unobscured flux during 2000–2016. Relation between the two parameters is indicated in Figure 9. We can see that the unobscured flux and the partial covering fraction are independent, which is reasonable since the former is determined by the inner accretion rate, and the latter represents the geometrical configuration of the clumpy absorbers.

5 CONCLUSION

We carried out a broad-band (0.3–78 keV) X-ray spectral analysis of NGC 5548 using the data obtained by *XMM-Newton*, *NuSTAR*, and *Suzaku* in 26 observations from 2000 to 2016. We have found that the long-term spectral variations are explained by the “variable double partial covering” (VDPC) model, where variations of the partial covering fraction due to double-layer clumpy absorbers account for most of the spectral variations (Figure 3). We propose a simple spectral variation model with only three variable components; the soft excess spectral component, the cut-off power-law normalization, and the partial covering fraction of the clumpy absorbers. Above ~ 1 keV, the observed flux/spectral variation is explained by two essentially variable parameters; the partial covering fraction and the cut-off power-law normalization, where the former dictates change

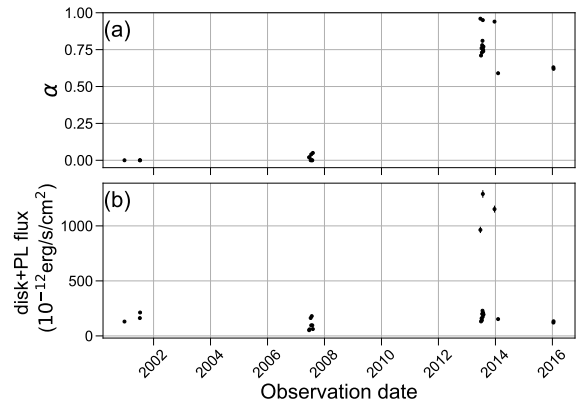


Figure 8. Parameter variations during 2000–2016 shown in Table 3: (a) covering fraction, (b) sum of the unobscured `diskbb` and `cutoffPL` fluxes.

of the spectral shape. In contrast, the intrinsic photon index and all the other spectral parameters are not significantly variable for over 16 years.

ACKNOWLEDGEMENTS

The authors gratefully thank the referee for critical comments to improve the paper. This research has made use of data and software provided by the High Energy Astrophysics Science Archive Research Center (HEASARC), which is a service of the Astrophysics Science Division at NASA/GSFC and the High Energy Astrophysics

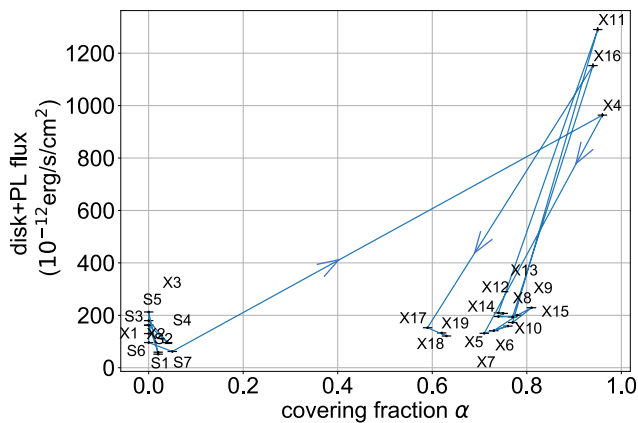


Figure 9. Partial covering fraction versus sum of the unobscured diskbb and cutoffPL fluxes. The arrow indicates the time order.

Division of the Smithsonian Astrophysical Observatory. This study was based on observations obtained with *XMM-Newton*, ESA science missions with instruments and contributions directly funded by ESA Member States and NASA. This research has made use of data obtained with the *NuSTAR* mission, a project led by the California Institute of Technology (Caltech), managed by the Jet Propulsion Laboratory (JPL) and funded by NASA. We utilized the public *Suzaku* data obtained by the Data ARchives and Transmission System (DARTS) provided by the Institute of Space and Astronautical Science (ISAS) at the Japan Aerospace Exploration Agency (JAXA). This research was supported by JSPS Grant-in-Aid for JSPS Research Fellow Grant Number JP20J20809 (T.M.), JSPS KAKENHI Grant Number JP16K05309 (K.E.) and JP21K13958 (M.M.). M.M. acknowledges support from the Hakubi project at Kyoto University. The authors acknowledge Ms. Juriko Ebisawa for proofreading and the artwork for Figure 3.

DATA AVAILABILITY

Observational data used in this paper are publicly available, and any additional data will be available on request.

REFERENCES

Antonucci R. R. J., Miller J. S., 1985, *ApJ*, 297, 621
 Arav N., et al., 2015, *A&A*, 577, A37
 Bekhti N. B., et al., 2016, *A&A*, 594, A116
 Cappi M., et al., 2016, *A&A*, 592, A27
 De Rosa G., et al., 2015, *ApJ*, 806, 128
 Di Gesu L., et al., 2015, *A&A*, 579, A42
 Done C., Davis S. W., Jin C., Blaes O., Ward M., 2012, *MNRAS*, 420, 1848
 Edelson R., Turner T. J., Pounds K., Vaughan S., Markowitz A., Marshall H., Dobbie P., Warwick R., 2002, *ApJ*, 568, 610
 Ferland G. J., et al., 2013, *Rev. Mex. Astron. Astrofis.*, 49, 137
 Hagino K., Odaka H., Done C., Gandhi P., Watanabe S., Sako M., Takahashi T., 2015, *MNRAS*, 446, 663
 Hagino K., Odaka H., Done C., Tomaru R., Watanabe S., Takahashi T., 2016, *MNRAS*, 461, 3954
 Harrison F. A., et al., 2013, *ApJ*, 770, 103
 Hirsch M., et al., 2019, *A&A*, 626, A64
 Iso N., Ebisawa K., Sameshima H., Mizumoto M., Miyakawa T., Inoue H., Yamasaki H., 2016, *PASJ*, 68, S27
 Jansen F., et al., 2001, *A&A*, 365, L1

Kaastra J. S., Mewe R., Liedahl D. A., Komossa S., Brinkman A. C., 2000, *A&A*, 354, L83
 Kaastra J. S., et al., 2014, *Science*, 345, 64
 Kallman T. R., Palmeri P., Bautista M. A., Mendoza C., Krolik J. H., 2004, *ApJS*, 155, 675
 Kobayashi H., Ohsuga K., Takahashi H. R., Kawashima T., Asahina Y., Takeuchi S., Mineshige S., 2018, *PASJ*, 70, 22
 Koyama K., et al., 2007, *PASJ*, 59, S23
 Krolik J. H., Kriss G. A., 2001, *ApJ*, 561, 684
 Krongold Y., et al., 2010, *ApJ*, 710, 360
 Laurenti M., et al., 2022, *A&A*, 657, A57
 Liu Y., et al., 2010, *ApJ*, 710, 1228
 Liu H., Luo B., Brandt W. N., Brotherton M. S., Gallagher S. C., Ni Q., Shemmer O., Timlin III J. D., 2021, *ApJ*, 910, 103
 Madsen K. K., Beardmore A. P., Forster K., Guainazzi M., Marshall H. L., Miller E. D., Page K. L., Stuhlinger M., 2017, *AJ*, 153, 2
 Maiolino R., et al., 2010, *A&A*, 517, A47
 Makishima K., Maejima Y., Mitsuda K., Bradt H. V., Remillard R. A., Tuohy I. R., Hoshi R., Nakagawa M., 1986, *ApJ*, 308, 635
 Matthews J. H., Knigge C., Higginbottom N., Long K. S., Sim S. A., Mangham S. W., Parkinson E. J., Hewitt H. A., 2020, *MNRAS*, 492, 5540
 Mehdipour M., et al., 2016, *A&A*, 588, A139
 Mehdipour M., et al., 2017, *A&A*, 607, A28
 Meyer-Hofmeister E., Meyer F., 2006, *A&A*, 449, 443
 Mitsuda K., et al., 1984, *PASJ*, 36, 741
 Mitsuda K., et al., 2007, *PASJ*, 59, S1
 Miyakawa T., Ebisawa K., Inoue H., 2012, *PASJ*, 64, 140
 Mizumoto M., Ebisawa K., 2017, *MNRAS*, 466, 3259
 Mizumoto M., Ebisawa K., Sameshima H., 2014, *PASJ*, 66, 122
 Mizumoto M., Ebisawa K., Tsujimoto M., Done C., Hagino K., Odaka H., 2019a, *MNRAS*, 482, 5316
 Mizumoto M., Done C., Tomaru R., Edwards I., 2019b, *MNRAS*, 489, 1152
 Nandra K., O’Neill P. M., George I. M., Reeves J. N., 2007, *MNRAS*, 382, 194
 Pancoast A., Brewer B. J., Treu T., Park D., Barth A. J., Bentz M. C., Woo J.-H., 2014, *MNRAS*, 445, 3073
 Petrucci P.-O., et al., 2013, *A&A*, 549, A73
 Pounds K. A., Reeves J. N., Page K. L., O’Brien P. T., 2004, *ApJ*, 605, 670
 Sobolewska M. A., Papadakis I. E., 2009, *MNRAS*, 399, 1597
 Soldi S., et al., 2014, *A&A*, 563, A57
 Starkey D., et al., 2017, *ApJ*, 835, 65
 Strüder L., et al., 2001, *A&A*, 365, L18
 Takahashi T., et al., 2007, *PASJ*, 59, 35
 Takeuchi S., Ohsuga K., Mineshige S., 2013, *PASJ*, 65, 88
 Urry C. M., Padovani P., 1995, *PASP*, 107, 803
 Ursini F., et al., 2015, *A&A*, 577, A38
 Whewell M., et al., 2015, *A&A*, 581, A79
 Williams P. R., et al., 2020, *ApJ*, 902, 74
 Wilms J., Allen A., McCray R., 2000, *ApJ*, 542, 914
 Yamasaki H., Mizumoto M., Ebisawa K., Sameshima H., 2016, *PASJ*, 68, 80
 den Herder J. W., et al., 2001, *A&A*, 365, L7

APPENDIX A: ENERGY SPECTRAL FITTING

As discussed in Section 3.3, we performed energy spectral fitting with all the available archival data. Figure A.1 and Figure A.2 show the results of the model fitting. The best-fit parameters are shown in Table 3.

This paper has been typeset from a $\text{\TeX}/\text{\LaTeX}$ file prepared by the author.

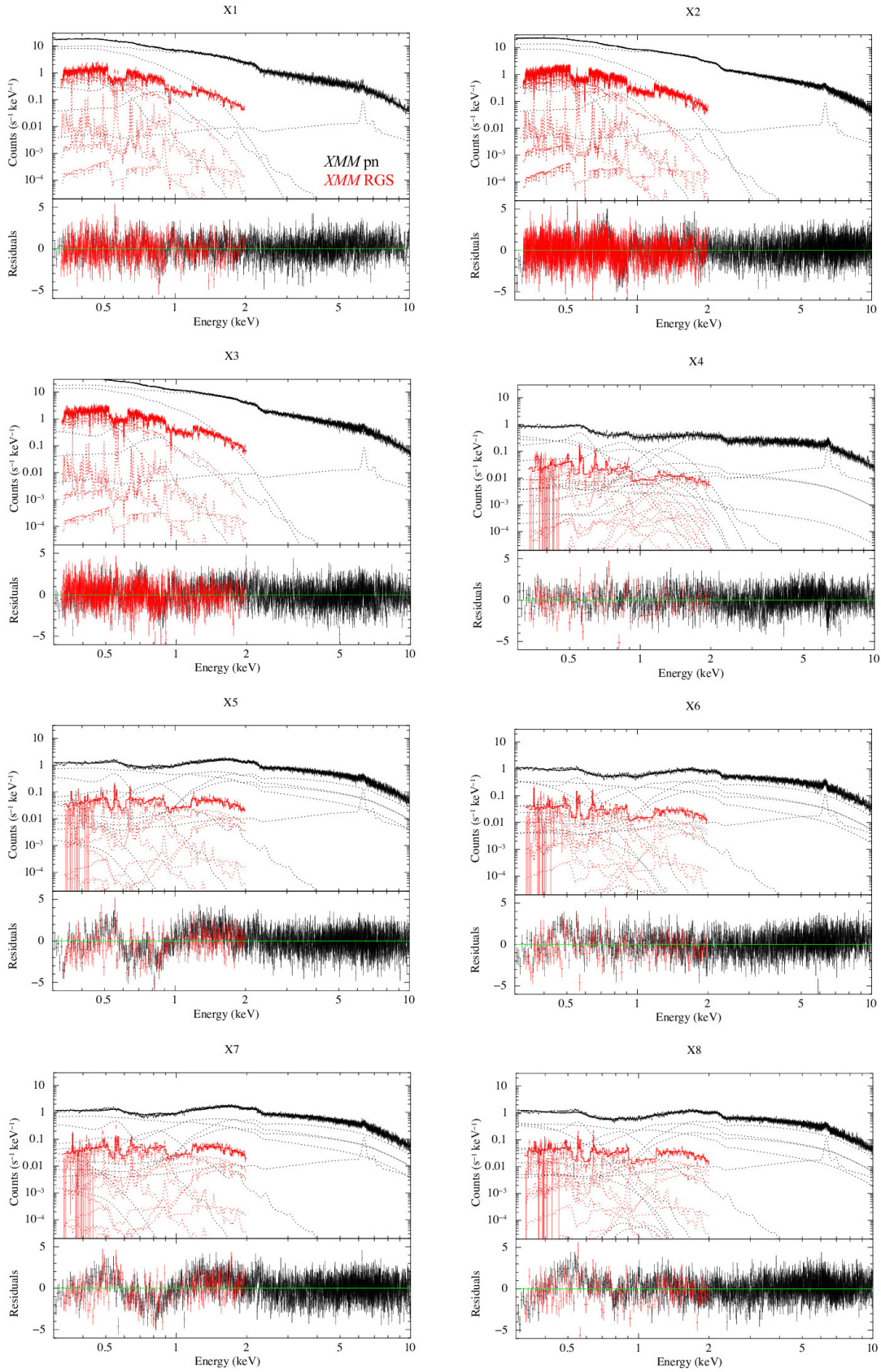


Figure A.1. Spectral fitting results of all the spectra taken by *XMM-Newton*. Black and red lines show the pn and RGS spectra, respectively. The vertical axes in both the panels are the same as those in Figure 4

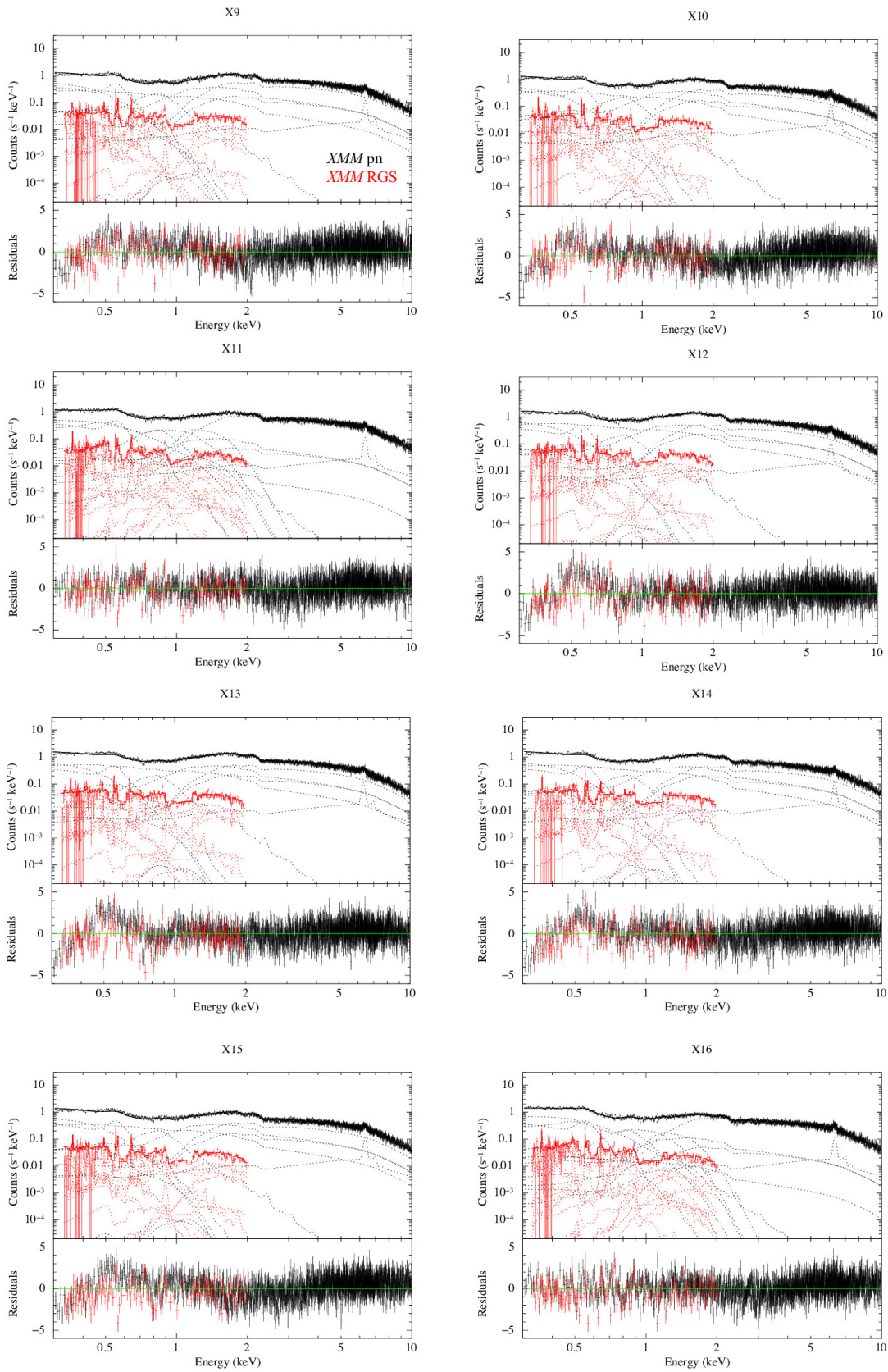


Figure A.1. Cont.

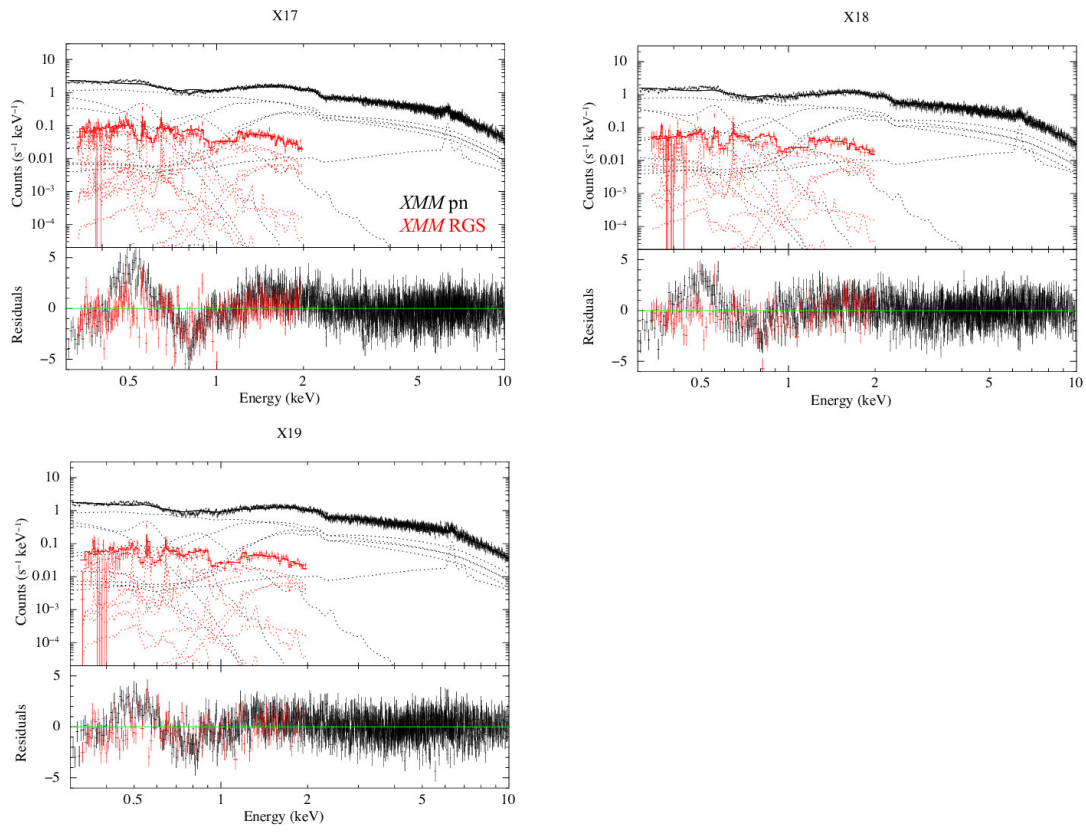


Figure A.1. Cont.

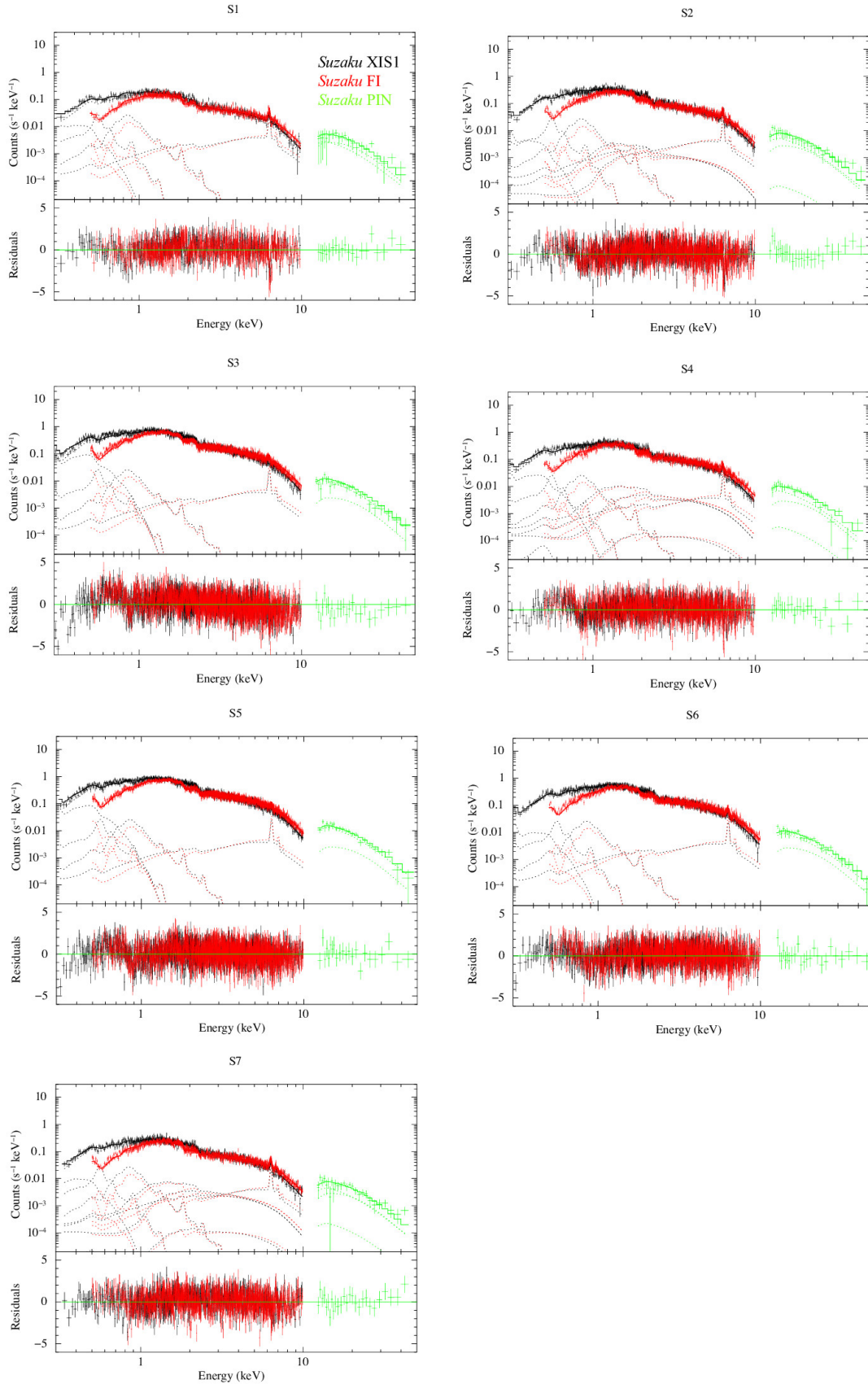


Figure A.2. Spectral fitting results of all the spectra taken by *Suzaku*. Black, red, and green lines show the XIS1, FI (XIS0&3), and PIN spectra, respectively. The vertical axes in both the panels are the same as those in Figure 4